Structures and energies of twist grain boundaries in Mg2SiO4 forsterite

Jean Furstoss, Pierre Hirel, Philippe Carrez, Karine Gouriet, Victoire Meko-Fotso, Patrick Cordier

Computational Materials Science 233 (2024) 112768

Contents lists available at ScienceDirect

Computational Materials Science

journal homepage: www.elsevier.com/locate/commatsci

Full length article

Structures and energies of twist grain boundaries in Mg_2SiO_4 forsterite

Jean Furstoss [a,*], Pierre Hirel [a], Philippe Carrez [a], Karine Gouriet [a], Victoire Meko-Fotso [a], Patrick Cordier [a,b]

[a] Univ. Lille, CNRS, INRAE, Centrale Lille, UMR 8207 - UMET - Unité Matériaux et Transformations, F-59000 Lille, France
[b] Institut Universitaire de France, 1 rue Descartes, F-75005 Paris, France

ARTICLE INFO

Dataset link: https://github.com/JeanFurstoss/AtomHIC

Keywords:
Twist grain boundaries
Silicate materials
Molecular static
Interface dislocations
Visualization in atomistic simulations

ABSTRACT

In this work, we investigate twist grain boundary (GB) energies and structures in Mg_2SiO_4 forsterite using atomistic simulations. We first present a new bond orientational order parameter allowing to highlight disordered regions in this low-symmetry crystal for which classical visualization tools are ineffective. Then we examine three GB planes, (010), (120) and (001), corresponding to the most favorable free surfaces of this crystal. We show that twist GB follow the same energy ordering as corresponding free surfaces. In addition, except for some misorientation angles and for the (120) GB plane, GB energies and structures are quite insensitive to microscopic translational degrees of freedom. The dislocation composition of low-angle twist GB can be related to γ-surfaces in the corresponding planes, and are in good agreement with first-principle calculations. It is also shown that the dislocation core structures in low angle twist GB can strongly differ from the ones of intracrystalline dislocations.

1. Introduction

Rocks are polycrystalline assemblies with properties conditioned not only by the properties of the individual crystals that compose them, but also to a large extent by the interfaces between these crystals: phase boundaries, and grain boundaries (GB) which will be the focus of this paper. Indeed, GB play critical roles in material, including rock, properties (e.g., mechanical [1,2], diffusional [3,4] or grain growth [5,6]) because of their atomic structures distinct from the bulk [7]. The description of GB is complex. Geometrically speaking alone, five macroscopic parameters must be specified to differentiate one GB from another. The lattice misorientation is described by three parameters, and the orientation of the GB plane is described by two parameters. The classic view that geometric parameters (in practice, most often only misorientation) are sufficient to define a GB and therefore to seek to define its properties is now being strongly challenged. While a ground state can always be defined, there are a multitude of metastable states [8] that play an important role on the properties. The microscopic degrees of freedom that add to these geometric parameters can be very complex in oxides [9,10] and even more in silicates. This complexity and multiplicity of structures gives rise to behaviors that exhibit the characteristics of phase transitions, for which the concept of complexion has been introduced [11,12]. As an illustration of the importance of that, recent studies (e.g. [13]) have cast doubt on the determinism of curvature and even of crystallography on GB mobility, suggesting a major role for microscopic structure (complexions). [14] have even shown that the presence of vacancies (i.e. a boundary between two crystals at thermodynamic equilibrium at finite temperature) enables other complexions to be reached. Note that the existence of amorphous boundaries can be seen as an extreme case of complexions [15]. Precise knowledge of the structure(s) of GB is therefore an essential prerequisite if we are ever to understand and model their properties.

In this study we focus on GB in a silicate, forsterite. Forsterite (Mg_2SiO_4) is the magnesium-rich end-member of the major constituent of the Earth's upper mantle, olivine. GB energies in olivine have been investigated experimentally for general boundaries [16] showing an increase of the energy with the misorientation angle until nearly 15° but poorly described by the Read and Shockley model [17]. HRTEM observations of forsterite GB remain scarce [18–20] and generally do not allow resolving their structure at the atomic scale. Atomistic simulations are thus the best-suited tools to investigate these defects. The diversity of configurations to be considered is a fundamental difficulty, and traditionally, efforts have focused primarily on simple cases such as tilt GB. Density functional theory (DFT) calculations have been used, for instance, to study energy and electronic structure of tilt GB in forsterite [21]. Structures and energies of a series of symmetrical tilt GB have also been investigated using a semi-empirical interatomic-potential approach by [22], showing that the studied low angle GB are composed by an array of partial edge dislocations.

* Corresponding author.
E-mail addresses: jfurstoss@orange.fr (J. Furstoss), pierre.hirel@univ-lille.fr (P. Hirel).

https://doi.org/10.1016/j.commatsci.2023.112768
Received 17 October 2023; Received in revised form 23 December 2023; Accepted 23 December 2023

Here we examine twist GB with the aim of extending our understanding of the nature of these defects towards general configurations. We focus on the three lowest energy planes of forsterite (010), (120) and (001) for misorientation angles ranging between 1 and 179°, completing part of the studied forsterite GB in the wide GB parameter space. Although never studied in a silicate like forsterite, twist GB have been widely investigated using molecular dynamics (MD) simulations. Regarding the structure of the low angle ones, a general observation is that they are composed of regular dislocation networks varying in size and shape with misorientation angle and GB plane [23–25]. It seems also common to observe dislocation dissociation and stacking faults within the structure of such type of GB [23,26]. In the following, a series of forsterite twist GB are studied using molecular static simulations. In order to analyze the GB structure and to identify the nature of defects present at the interfaces, we rely on a new order parameter developed to overcome the intrinsic limitations of centro-symmetry parameter or common neighbor analysis in case of low symmetry crystals. Finally, the defect structures are highlighted against the energy landscapes of the sampled planes and an analytical model describing the evolution of GB energy as function of misorientation angle for low angle twist GB is set up.

2. Methodology

2.1. Computation techniques

Inter-ionic interactions are described by the rigid-ion potential from Pedone and co-workers [27], including long-range Coulomb interactions, and short-range interactions described by a truncated Lennard-Jones function (i.e. a repulsive r^{-12} term) and a Morse function. Partial charges are $q_O = -1.2e$ for oxygen ions, and $q_{Mg} = 1.2e$ and $q_{Si} = 2.4e$ for Mg and Si ions respectively. Coulomb interactions are computed using the particle–particle/particle–mesh (pppm) method [28], which decomposes short- and long-range contributions in real and reciprocal space respectively. Numerous physical properties of forsterite including bulk, surfaces and defects properties are well described by this potential [29]. Moreover, this potential was shown to be in good agreement with density functional theory (DFT) calculations regarding energies and structures of a forsterite symmetrical tilt GB [30]. In the following, all simulations are performed using LAMMPS [31]. Energy minimization is performed with the conjugate-gradient algorithm. All presented GB structures are the result of energy minimization, and are obtained without accounting for the effects of temperature or pressure (0 GPa).

2.2. Grain boundaries initial configurations and energy calculation

We begin with cells of Mg_2SiO_4, taken from the work of Bruno et al. [32], where the free (010) surface (respectively (001) and (120) surfaces) lies normal to the Cartesian Z axis. Two crystals with the same orientation are then rotated around the Z axis by opposite angles of $\theta/2$ and $-\theta/2$. The complexity of the orthorhombic lattice does not allow to construct exact coincidence site lattice (CSL). Hereafter, we search for linear combinations of lattice vectors orthogonal to GB plane normal, that yield final cell vectors aligned with Cartesian X and Y axes with a tolerance of 0.1°. These linear combinations are used to duplicate the unit cells and obtain two orthogonal grains with the same dimensions and with a twist misorientation $\theta \pm 0.1°$. This methodology allows to construct the GB with a low near-Σ values, while keeping the number of ions as small as possible. Finally, we stack the two grains on top of one another, leading to the initial atomic configuration of (010) twist GB (respectively (001) and (120) GB). To handle periodic boundary condition along the Z axis, vacuum layers are introduced on both sides of the system. We then perform a full energy minimization of volume and ion positions. As built, the energies of the free surfaces created by the insertion of vacuum have to be accounted for in the calculation of the GB energy γ:

$$\gamma(\theta) = E^{2N}(\theta) - E^{2N}_{\text{bulk}} - 2E_{(hkl)} \tag{1}$$

where E^{2N} is the potential energy of the system of $2N$ atoms containing the GB, E^{2N}_{bulk} is the potential energy of a relaxed single crystal with the same number of atoms, and $E_{(hkl)}$ is the potential energy of the corresponding free surface, with (hkl) =(010), (001), or (120). The latter energy term is computed as the difference between the energy of a single crystal, and that of one with free surfaces. It is worth noticing that our previous work has shown that the Pedone potential reproduces free surface energies with a good accuracy [29]. Using this methodology, the energy $E_{(hkl)}$ does not depend on θ, and we find that a total height of 60 Å along Z for the bicrystal yields converged values for both surface and GB energies.

A series of twist GB are constructed following the above described methodology for three different GB planes, (010), (120) and (001). Since the forsterite structure does not have mirror planes, we sample misorientation angles θ from 1° up to 180° with a step of 1°. Systems containing more than 600000 ions have been discarded for computational efficiency. In order to sample a part of the microscopic degrees of freedom, we generate 25 initial configurations for each GB plane and misorientation, corresponding to different translations between the two grains within the GB plane (5 different translations in each direction).

2.3. Elastic models of low-angle grain boundaries

As low-angle GB are expected to be composed of array of dislocations, their energies can be modeled using the elastic theory of dislocation. The Read–Shockley model [17], initially built to describe low-angle tilt GB energies, is adapted for low-angle twist GB [33] :

$$\gamma_{\text{th}} = \frac{\mu b^2}{2\pi}\theta\left(1 + \ln\frac{b}{2\pi r_c} - \ln\theta\right) \tag{2}$$

where μ is the shear modulus of the crystal and b and r_c are the Burgers vector and core radius of the dislocations composing the GB respectively.

In the case where multiple dislocation types are present, this expression no longer holds and a model accounting for the different dislocation types must be used [34] :

$$\gamma_{\text{th}} = \frac{\mu}{4\pi}\sum_{i=1}^{2}\frac{b_i^2}{d_i}\ln\left(\frac{d_i}{r_c^i}\right) \tag{3}$$

where d_i is the spacing between dislocation of type i. These distances can be computed for general GB using the Frank–Bilby equation [35–37], and can be simplified for pure tilt and pure twist GB using [38] :

$$d_i = \frac{b_i}{2\sin(\theta/2)} \tag{4}$$

In the case where dislocations dissociate in the GB, the created stacking fault (SF) has an energy γ_{SF} contributing to the GB energy. Eq. (3) is then modified [26]:

$$\gamma_{\text{th}} = f_{SF}\gamma_{SF} + \frac{\mu}{2\pi}\sum_{i=1}^{2} b_i\sin(\theta/2)\ln\left(\frac{b_i}{2\sin(\theta/2)r_c^i}\right) \tag{5}$$

where f_{SF} is the faulted area fraction of the GB.

2.4. Bond orientational order parameter

Due to the complex chemistry and crystallography of a silicate like forsterite, visualization of defects is a challenging task, requiring advanced numerical methods. Those that are robust in cubic and/or centro-symmetric materials, such as centro-symmetry criterion [39], common neighbor analysis [40], or dislocation extraction analysis (DXA) [41], do not yield exploitable results in the forsterite structure.

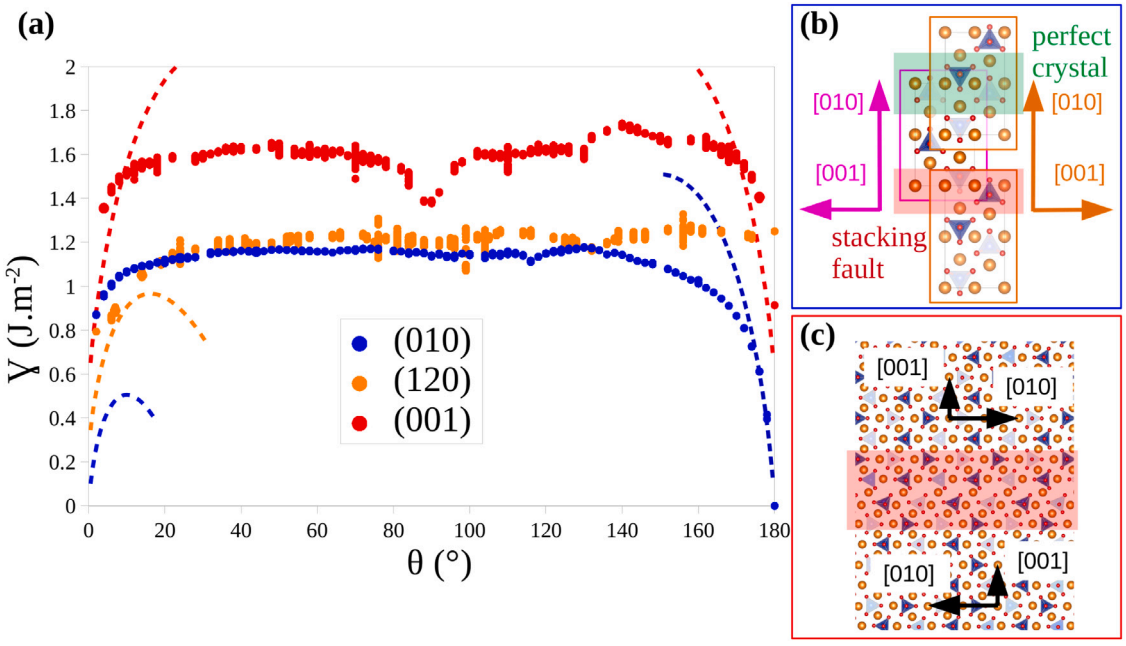

Fig. 1. (a) Interfacial energies as function of the twist angle between the two grains for (010) (blue), (120) (orange), and (001) GB (red). Dots are energies obtained from atomistic simulations, and dashed lines represent theoretical GB energies γ_{th} presented in Section 2.3. (b) When the two crystals are rotated by 180° around [010], they may form a stacking fault (red area), or perfect crystal if the top grain is appropriately translated (green area). (c) When the two crystals are rotated by 180° around [001], it is not possible to retrieve perfect crystal, and the two grains form a stacking fault (red area).

Indeed, in forsterite not only none of the sub-lattices have a central symmetry, but also Mg or O ions occupy different non equivalent crystallographic sites. As a result, we introduce a specific order parameter based on spherical harmonics and local neighborhood environment through the use of Steinhardt's parameters [42]. These rotationally and translationally invariant parameters can be expressed as:

$$q_l^i = \sqrt{\frac{4\pi}{2l+1}\sum_{m=-l}^{l}\left|q_{lm}^i\right|^2} \tag{6}$$

where,

$$q_{lm}^i = \frac{1}{\left|N^i(r_c)\right|}\sum_{j=1}^{N^i(r_c)} Y_{lm}(\theta_{ij},\phi_{ij}) \tag{7}$$

where $N^i(r_c)$ represents the neighboring ions of ion i inside a given cutoff radius r_c, Y_{lm} are the spherical harmonics and θ_{ij} and ϕ_{ij} are the colatitude and azimuthal angles between ions i and j, respectively.

Following the work of [43,44], one can define:

$$Q_{lm}^i = \frac{\sqrt{4\pi}}{q_l^i\left|N^i(r_c)\right|\sqrt{2l+1}}\sum_{j=1}^{N^i(r_c)} Y_{lm}(\theta_{ij},\phi_{ij}) \tag{8}$$

which at the difference with q_{lm}^i has the property to be square-normed (i.e. $\sum_{m=-l}^{l}\left|Q_{lm}^i\right|^2 = 1$). Then, in order to measure the similarity of the ion i with respect to its local neighborhood we define, for a given l value, the un-normalized order parameter:

$$o^i = \frac{1}{\left|S^i(r_c)\right|}\sum_{k=1}^{S^i(r_c)}\left(\sum_{m=-l}^{l} Q_{lm}^i Q_{lm}^{k\,\star}\right) \tag{9}$$

where $S^i(r_c)$ represents the neighboring ions having the same crystallographic site of ion i inside the cutoff radius r_c. The crystallographic sites are determined using the comparison between the Steinhardt parameter q_l^i and some reference Steinhardt parameters q_l^s, previously computed on a perfect crystal unit cell of forsterite. In practice, the site s is affected to the ion i of type t_i to the site corresponding to the smallest $\left|q_l^s(type = t_i) - q_l^i\right|$.

As forsterite crystal is not centrosymmetric, the values of o^i even for perfect crystal sites are not equal to 1. The final order parameter $\mathcal{O}^i$ is then obtained following:

$$\mathcal{O}^i = 1 - o^i/o^s \tag{10}$$

where o^s is the reference un-normalized order parameter for the crystallographic site of ion i. As for q_l^s, these parameters are previously computed for a perfect crystal unit cell of forsterite. This final order parameter is worth 0 when the ion is in a perfect crystal environment and goes to 1 when the neighborhood is randomly dispersed. Between these two latter cases, the order parameter is closer to 0, even in a non-perfect crystal environment, in an area where the ions of the same type and site inside the cutoff radius have a similar neighborhood, for instance in a SF.

It is worth mentioning that all parameters presented in this section depends on cutoff radius r_c and spherical harmonic degree l. The reference parameters q_l^s and o^s have then to be computed using the same r_c and l as for Q_{lm}^i and o^i. For the forsterite crystal, we find that values of 7.5 $\mathring{A}$ and 20 for r_c and l respectively, give satisfactory results (i.e. close to one for ions in perfect crystal environment and going to zero for amorphous environment).

Construction of GB atomic systems as well as computation of bond orientational order parameter were performed using the home-made code "AtomHIC" (https://github.com/JeanFurstoss/AtomHIC).

2.5. Disregistry

To further characterize GB dislocations and their Burgers vectors, we compute the disregistry between the two atomic planes joining the GB. Disregistry is defined as the relative displacement of atoms in one plane with respect to the other [45]. Due to the complexity of the forsterite crystal, only silicon ions are used to compute the disregistry. We find that displacements normal to the GB plane is negligible, and only in-plane components will be presented hereafter.

Once the atomic disregistry is extracted from an atomic configuration, we fit it with a function of the form [45]:

$$\varphi(\mathcal{X}) = \frac{b}{\pi}\left(\arctan\frac{\mathcal{X}-\mathcal{X}_D}{r_c} + \frac{\pi}{2}\right) \tag{11}$$

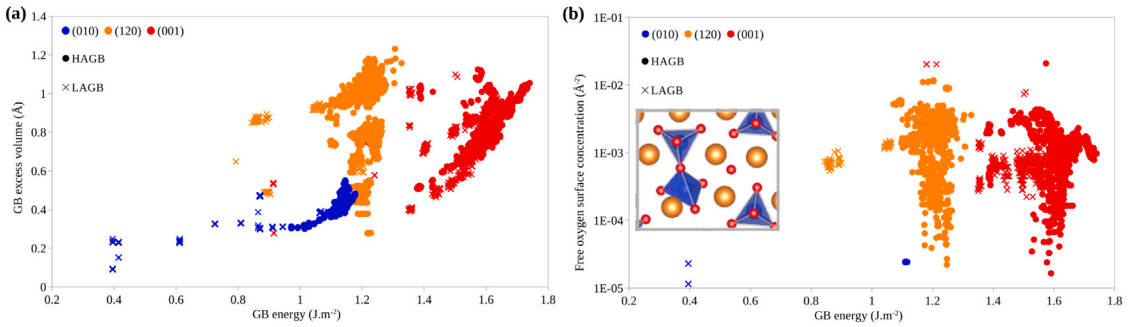

Fig. 2. GB excess volume (a) and free oxygen concentration (b) as a function of GB energy, crosses and circles represent low and high angle GB, respectively. The logarithmic scale in (b) does not allow representing a null concentration which is the case for most of the (010) GB.

where $\mathcal{X}$ is a spatial coordinate and $\mathcal{X}_D$ is the dislocation position. Fitting variables are the dislocation position $\mathcal{X}_D$, and dislocation core radius r_c. The latter is then used as an input parameter to compute the theoretical GB energy (see Section 2.3).

3. Results

3.1. Grain boundary energies, excess volume and free oxygen

Fig. 1(a) presents interfacial energies γ corresponding to (010), (120), and (001) GB planes, as a function of the misorientation θ. In all cases, the GB energy increases smoothly for small-angle GB ($0° \leq \theta \leq 20°$), and reaches an energy plateau for larger misorientations, approximately 1.17 J·m^{-2} for (010) GB, 1.2 J·m^{-2} for (120), and 1.6 J·m^{-2} for (001). These values can be related to the free surface energies, which are $\gamma^{(120)} = 1.07$, $\gamma^{(010)} = 1.10$, and $\gamma^{(001)} = 1.49$ J·m^{-2} [29]. We find that the ratio between GB energies is comparable to ratio between free surface energies.

As the misorientation approaches 180°, GB energies tend to decrease. However, because there is no mirror symmetry plane in the forsterite structure, two crystals rotated by 180° around a shared axis do not necessarily form a perfect crystal. In the case of rotation around [010] axis, they may form a perfect crystal if the top grain is translated with respect to the bottom one (Fig. 1(b)). As a result, the GB energy drops to zero when reaching $\theta = 180°$ (blue dots in Fig. 1(a)). In the case of the [001] axis, it is not possible to retrieve a perfect crystal, and the two grains form a SF with an energy of around $\gamma^{\pi}_{(001)} \approx 0.91$ J·m^{-2} when $\theta = 180°$ (red dot in Fig. 1(a)). Finally, in the case of a rotation around the normal of (120), the two crystals rotated by 180° form a SF with a higher energy $\gamma^{\pi}_{(120)} \approx 1.2$ J·m^{-2}, i.e. comparable to the energies of high-angle (120) GB.

Noticeably, none of the curves present cusps (i.e. particular angles for which the GB energy would drop significantly), at the exception of (001) GB near $\theta \approx 90°$. This particular twist angle corresponds to a near $\Sigma 105$ GB with an energy of 1.35 J·m^{-2}. For a given GB plane and misorientation angle, the energies of high-angle GB have a dispersion smaller than 0.05 J·m^{-2}, due to the relative position of the two crystals. This indicates that the twist GB energies are insensitive to the relative translations between adjacent crystals investigated here. In contrast, the type or index of the GB plane (e.g. (010) vs (001)) is responsible for much larger energy differences.

As shown in sections below, the structures of low angle GB have been systematically examined using the order parameter (Section 2.4). A part of the high angle GB (for twist angles higher than 20° and lower than 160°) obtained after relaxation has been examined in the light of the order parameter but neither particular feature nor periodic patterns have been observed.

The excess volume for each GB has been computed using the formulae presented in [30] and is presented in Fig. 2(a). For (010) and (001) cases, the GB excess volume and energy are positively correlated for both low and high angle twist GB. For the (120) case, there is no clear correlation between excess volume and energy.

As linked SiO_4 tetrahedra and free oxygen ions have been observed in tilt GB in forsterite by [30], the concentration of free oxygen per GB unit surface has been computed as shown in Fig. 2(b). For (001) and (120) GB, the concentrations range between 10^{-5} and 10^{-2} Å^{-2} for mean values of $1.3 \cdot 10^{-3}$ and $1.9 \cdot 10^{-3}$ Å^{-2}, respectively. This atomic feature is not correlated with GB energy neither for low nor high angle ones. Free oxygen and linked SiO_4 tetrahedra are almost never found in (010) GB.

3.2. Low-angle twist grain boundaries

In low-angle twist GB, the misorientation is typically accommodated by an arrangement of geometrically necessary dislocations (GNDs) of screw character. As the misorientation angle increases, the dislocation lines come into close proximity and exhibit significant interactions, eventually reaching a critical angle beyond which it becomes impossible to distinguish individual dislocations. In this section, we focus on low-angle and near-180° twist GB, allowing us to observe and characterize the defect composing them.

3.2.1. (010) plane

We start by examining the case of a 2° (010) twist GB, as shown in Fig. 3(a). The bond orientational order parameter (Eq. (10)) reveals the presence of two distinct linear defects oriented orthogonally to each other. These defects, primarily aligned with the [100] and [001] directions, are not fully rectilinear and appear to extend within the GB plane. By calculating disregistries, we can identify two types of dislocations.

Firstly, we observe screw dislocations with [100] Burgers vectors, and the fitting process (Eq. (11)) provides a core width of approximately 14 Å, which is roughly equivalent to 3 unit cells along the [001] direction (Fig. 3(b)). In the vicinity of the dislocation core, there is a small edge component in the disregistry function, which diminishes at longer ranges (blue curves).

Secondly, we identify screw dislocations with [001] Burgers vectors, and their core width ranges between 7 and 13 Å, corresponding to 2 to 3 unit cells along the [100] direction (Fig. 3(c)).

We now examine the near-180° (010) GB. As mentioned earlier, when the top crystal is rotated by 180° around the [010] axis, it can form a perfect crystal through appropriate translation. Therefore, when the misorientation deviates from 180°, it accommodates this deviation through an array of GND, making this type of GB behave like a low-angle GB.

In Fig. 4(a), we observe the atomic structure of the 178° (010) GB, which appears to contain dislocations along [100] and [001], similar to the 2° GB discussed earlier. However, the computation of disregistries reveals that these dislocations have spread much less, as seen in Fig. 4(b,c). Screw dislocations with [100] Burgers vectors have

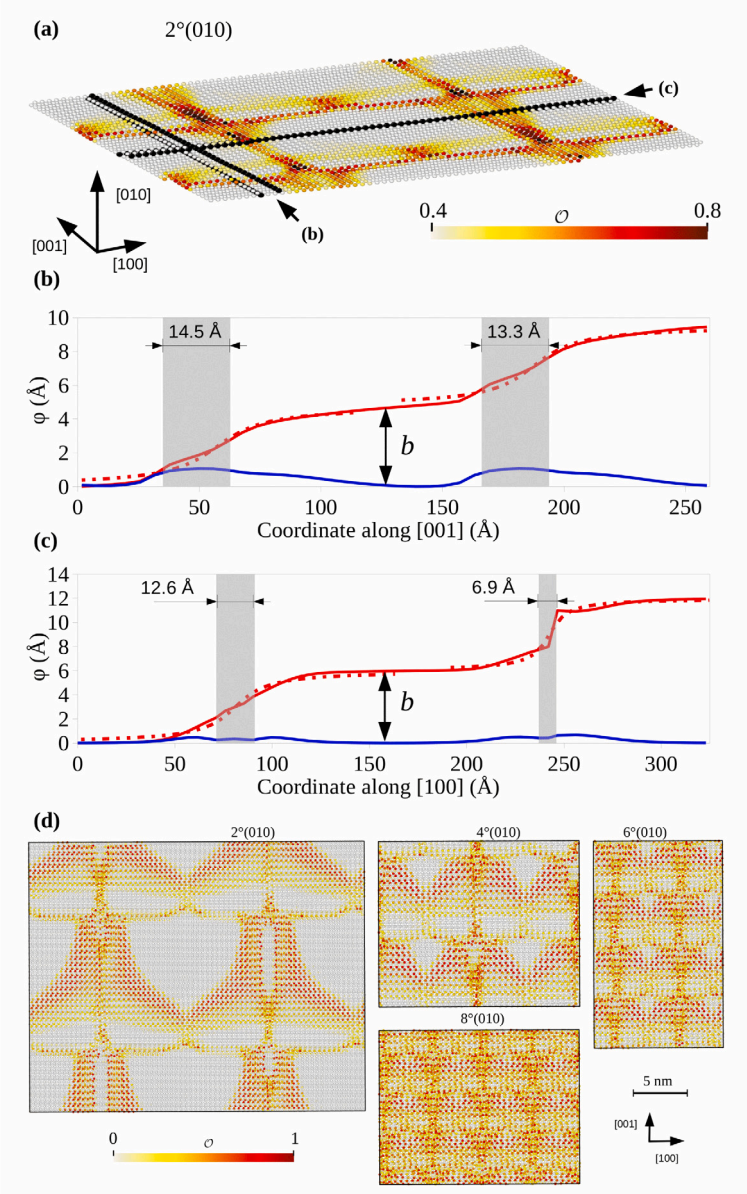

Fig. 3. Visualization and characterization of low-angle (010) twist GB. (a) Visualization of the two atomic planes in the vicinity of the 2°(010) GB. Only Si ions are represented, and colored according to the order parameter (Eq. (10)). Black lines indicate the atomic columns used to compute the disregistries φ. (b) Disregistry measured along [001] (solid lines), showing the screw (red) and edge (blue) components of two dislocations with [100] Burgers vectors. The fitted function (Eq. (11)) is represented with a dashed line, and gray regions emphasize the location and core width (r_c). (c) Disregistry measured along [100] (same color code as (b)). Here the two screw dislocations have [001] Burgers vectors. (d) Top-view of other low-angle (010) twist GB colored according to the order parameter, all ion types are represented.

a core width of approximately 1.9 Å, while [001] dislocations have a core width of 6.8 Å. Furthermore, the edge component in the vicinity of dislocations is also significantly smaller compared to the previous case.

3.2.2. (001) plane

Fig. 5(a) shows the structure of the 4° (001) low-angle twist GB. Once again, the bond orientational parameter aids in visualizing two distinct types of linear defects, which we have characterized through the calculation of their disregistry functions.

The first category of defects corresponds to perfect screw dislocations featuring [100] Burgers vectors. These dislocations exhibit a compact core width, typically ranging from 2 to 3 Å, and they are interspersed by regions of pristine crystalline structure (Fig. 5(c)).

The second type of dislocations is fragmented into partial screw dislocations possessing colinear Burgers vectors, specifically $b_1 = b_2 = \frac{1}{2}[010]$. These partial dislocations are separated alternately by regions of perfect crystal and intrinsic stacking faults (ISF). The presence of ISF is associated with a non-zero bond-order parameter, resulting in the appearance of atoms within ISF in yellow (see blue arrows in Fig. 5(a)).

The atomic structure of this ISF is elucidated in Fig. 5(b), illustrating a translation of a segment of the crystal by a vector of $\frac{1}{2}[010]$. Subsequently, we crafted a simulation cell exclusively containing this ISF, and energy minimization elucidated its status as a metastable SF with an interfacial energy of approximately $\gamma^{\mathrm{ISF}}_{(001)} = 1.06\ \mathrm{J{\cdot}m^{-2}}$.

Examination of disregistries within the (001) GB delineates that the $\frac{1}{2}[010]$ partial dislocations exhibit remarkable narrowness, spanning from 2.2 to 6 Å, and are divided by a distance of approximately 60 Å, with the ISF occupying the intervening space (Fig. 5(d)).

We now turn to near-180° (001) GB. As explained earlier, when the two crystals are rotated by 180° around [001], it is not possible to retrieve perfect crystal. Instead, the system contains a SF, different

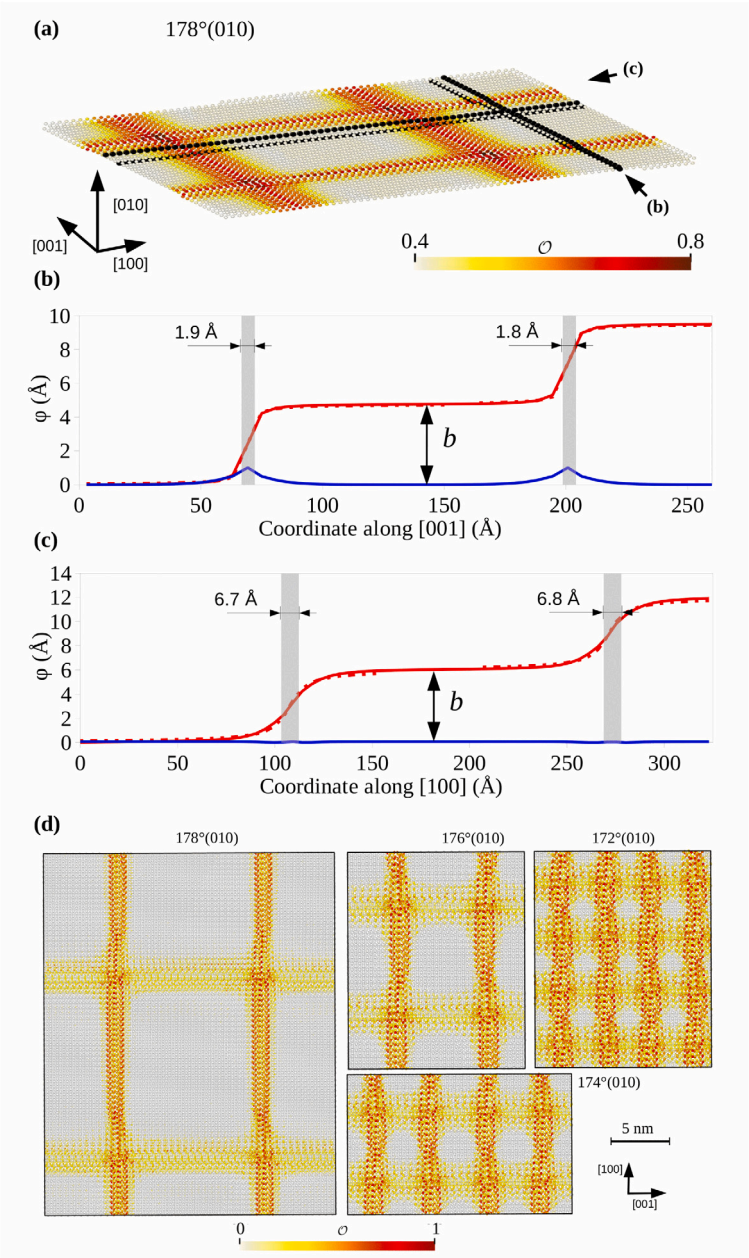

Fig. 4. Visualization and characterization of near-180° (010) twist GB. (a) Visualization of the two atomic planes in the vicinity of the 178°(010) GB (same color code as Fig. 3). (b,c) Disregistries corresponding to (b) [100] and (c) [001] screw dislocations in the GB plane. (d) Top-view of other near-180° (010) twist GB (same color code as Fig. 3).

from the previous one, which we name $\pi(001)$ SF, and is represented in Fig. 6(b). That is why at $\theta = 180°$ the GB energy does not vanish (Fig. 1), but has a residual value corresponding to the energy of this SF, $\gamma^{\pi}_{(001)} = 0.91$ J·m^{-2}.

When deviating from 180°, in addition to the $\pi(001)$ SF, the GB also contains an array of GND. Fig. 6(a) shows the atomic structure of the 176° (001) GB, where the bond-order parameter allows to visualize the $\pi(001)$ SF (in yellow), and two types of line defects (in red). Computation of the disregistries allows their identification as screw dislocations with [100] and [010] Burgers vectors, respectively. Like in the previous low-angle GB, [010] dislocations are split into colinear partials $\frac{1}{2}[010]$. Since the GB plane is entirely covered by a $\pi(001)$ SF, the dissociation of [010] dislocations introduces an additional SF. This new type of SF is associated with rotation of the top crystal by 180° around [001], and translation by $\frac{1}{2}[010]$, so we name it $\pi b/2(001)$ SF. It is associated with an energy $\gamma^{\pi b/2}_{(001)} = 1.18$ J·m^{-2}.

3.2.3. (120) plane

Finally, we investigate low-angle (120) twist GB. Fig. 7(a) shows the microstructure of the (120) GB with a misorientation $\theta = 2°$. The atom coloring, based on the bond-order parameter, unveils a considerably more intricate configuration compared to the previous (010) or (001) GB. In this case, extensive regions exhibit non-zero values of the parameter. Furthermore, several linear defects can be discerned, some aligned with the [001] direction, and others parallel to $[\bar{2}10]$ with varying separation distances.

Computation of disregistries confirms that the first category of defects, aligned with [001], is screw dislocation with [001] Burgers

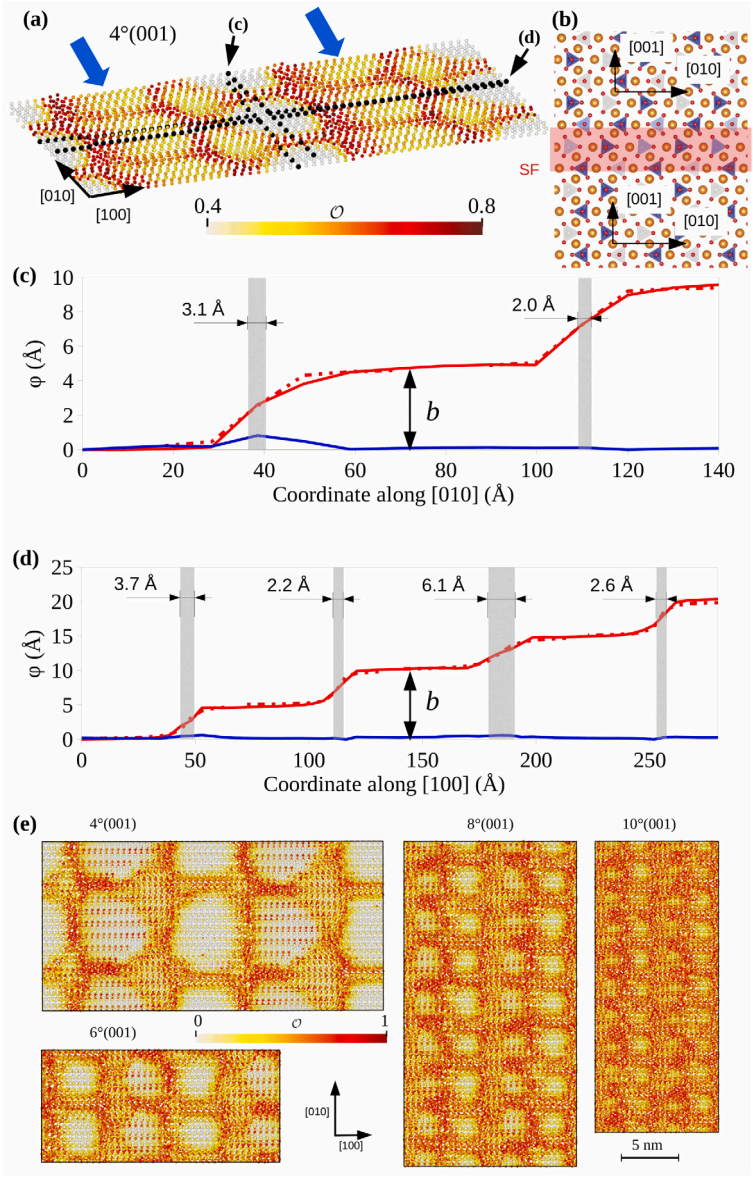

Fig. 5. Visualization and characterization of low-angle (001) GB. (a) Visualization of the 4° (001) GB (same color code as Fig. 3). Regions where atoms appear in white correspond to perfect crystal, those in yellow, highlighted by the blue arrows, to the intrinsic stacking fault (ISF) presented in (b). Black lines show the atomic columns used to compute the disregistries φ presented in (c) and (d). (b) Atomic view of the $\frac{1}{2}[010](001)$ ISF, corresponding to yellow regions in (a). (c,d) Disregistries in the GB plane corresponding to (c) [100] and (d) [010] screw dislocations. (e) Top-view of other low-angle (010) twist GB (same color code as Fig. 3).

vectors (Fig. 7(c)). These dislocations exhibit an average core width of approximately 8.8 Å and are separated by distances of 180 Å.

The second family of dislocations, aligned with $[\bar{2}10]$, show a much more complex pattern, as reported in Fig. 7(d). We identify a first group of four dislocations, spreading from 30 Å to 220 Å, and a second group spreading from 410 to 600 Å. Both groups share the same features. The four dislocations are of screw character with Burgers vectors $\frac{1}{4}[\bar{2}10]$, so that in total they amount to a perfect $[\bar{2}10]$ lattice vector. They have very narrow core widths about 3.1 Å on average.

The $\frac{1}{4}[\bar{2}10]$ partial dislocations are not uniformly spaced and are interspersed with two smaller SF and one larger SF. The atomic structure of this SF is illustrated in Fig. 7(b). To further characterize this SF, we constructed a simulation cell solely dedicated to its examination, and the computed energy for this configuration amounts to $\gamma^{SF}_{(210)} = 0.49\ J{\cdot}m^{-2}$. The two smaller SF have not been explicitly modeled in our study.

The structure of near-180° (120) twist GB do not exhibit visible linear defects or particular features and are thus not presented.

Dislocation core radii and energies of different SF obtained in our simulations are summarized in Table 1.

4. Discussion

4.1. Low angle GB: GB dislocations, generalized stacking faults

As expected from the geometrical constraints of low angle twist boundaries, all low-angle boundaries investigated here consist of two sets of dislocations with screw characters, with Burgers vectors along [100], [010], [001] or $[\bar{2}10]$, intersecting each other in the grain boundary plane. These dislocations should be regarded as interface GND, associated with the plane to which they belong, and distinct from their intracrystalline counterparts.

Firstly, whereas dislocations with [100] and [001] Burgers vectors are commonly found experimentally in forsterite crystal [46,47] as well as in (010) twist low angle GB [48–50], it seems clear from our results that their structures could change depending on the context. Indeed,

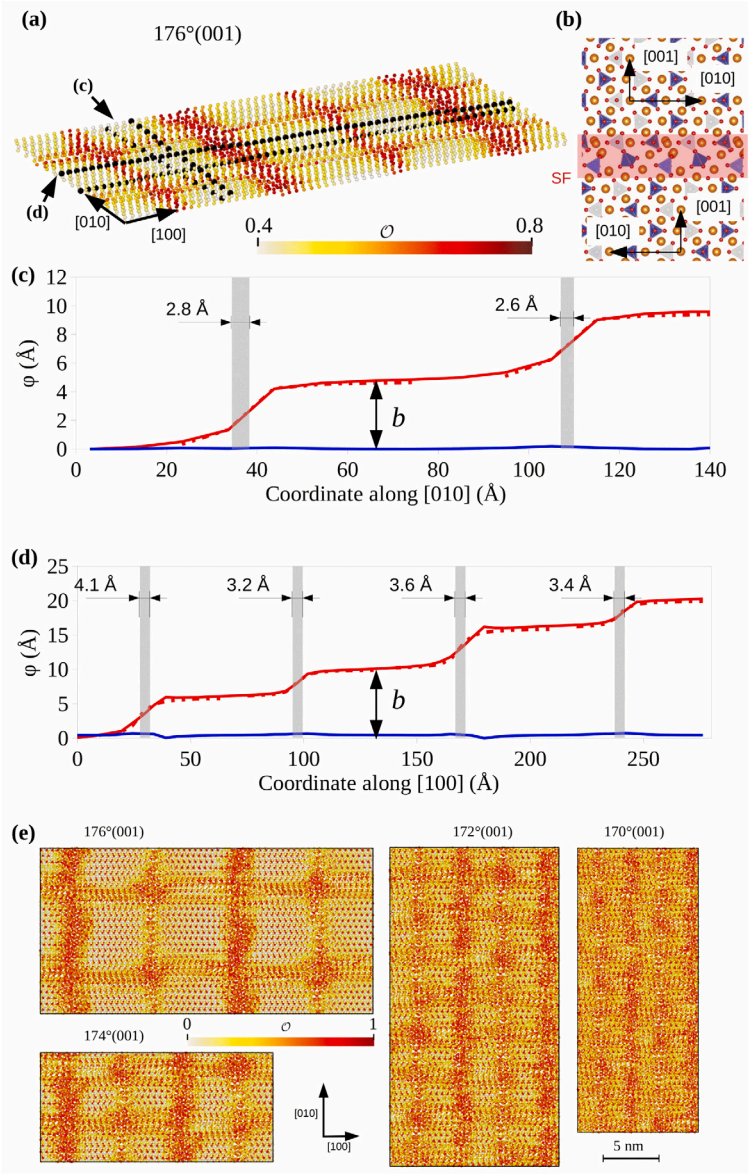

Fig. 6. Visualization and characterization of near-180° (001) twist GB. (a) Visualization of the 176° (001) GB (same color code as Fig. 3). Black silicon ions indicate atomic columns used to compute the disregistries φ presented in (c) and (d). (b) Atomic representation of the π (001) SF resulting from rotation of the top crystal by 180° around [001]. This SF appears in yellow in other figures. (c) Disregistry associated with [100] screw dislocations. (d) Disregistry associated with [010] dislocations. (e) Top view of other near-180° (001) GB.

Table 1
Values of dislocation core widths (r_c) and stacking fault energies (γ) obtained from atomistic simulations, and used in the elastic model to compute GB energy (see Eq. (5) and Section 2.3). Values in parenthesis are the standard deviations. $\gamma^{\pi}_{(001)}$ is the minimum energy of the stacking fault created by a rotation of 180° around the twist axis. In the case of (001) GB, the second value corresponds to the $\pi b/2(001)$ SF (see text).

	(010) 2° and 178°	(001) 4° and 176°	(120) 2°
$r_c^{[100]}$ (Å)	13.9(0.9) – 1.9(0.0)	2.6(0.7) – 2.7(0.1)	–
$r_c^{[001]}$ (Å)	9.7(4.0) – 6.8(0.1)	–	8.8(1.3)
$r_c^{\frac{1}{2}[010]}$ (Å)	–	3.6(1.8) – 3.6(0.4)	–
$r_c^{\frac{1}{3}[\bar{2}10]}$ (Å)	–	–	3.1(2.2)
γ^{ISF} (J·m^{-2})	0.00	1.06	0.49
γ^{π} (J·m^{-2})	0.00	0.91, 1.18	1.25

the core of the interface GND studied here are widely spread in the GB plane, leading to two distinct core structures of the [100] interface GND in (010) and (001) low angle twist GB. Moreover, these interface GND are also much different than the intracrystalline [100] dislocations which have a narrower and extended in (010) core structure [51]. The [001] interface GND also differ from the intracrystalline ones having a much narrower structure, and mostly spread in {110} planes [52].

Secondly, the dissociation reaction of the [010] Burgers vector in (001) low angle twist GB (i.e. [010] = 1/2[010] + 1/2[010]) differs from the ones characterized in the bulk by [53] such that [010] = 1/4[01$\bar{1}$]+1/4[01$\bar{1}$]+1/4[011]+1/4[011] and [010] = 1/4[01$\bar{1}$]+1/4[01$\bar{1}$]+1/2[011]. Furthermore, perfect [010] dislocations have been identified in low angle GB [48,54], which contrasts with the dissociation behavior observed in our simulations.

Lastly, dislocations with Burgers vectors along [$\bar{2}$10] have not been observed either experimentally in the bulk or in GB contexts.

To push forward the understanding of these differences between interface GND and intracrystalline dislocations, as well as between different types of interface GNDs, a more detailed analysis of dislocation core structures is required. While the generalized stacking fault

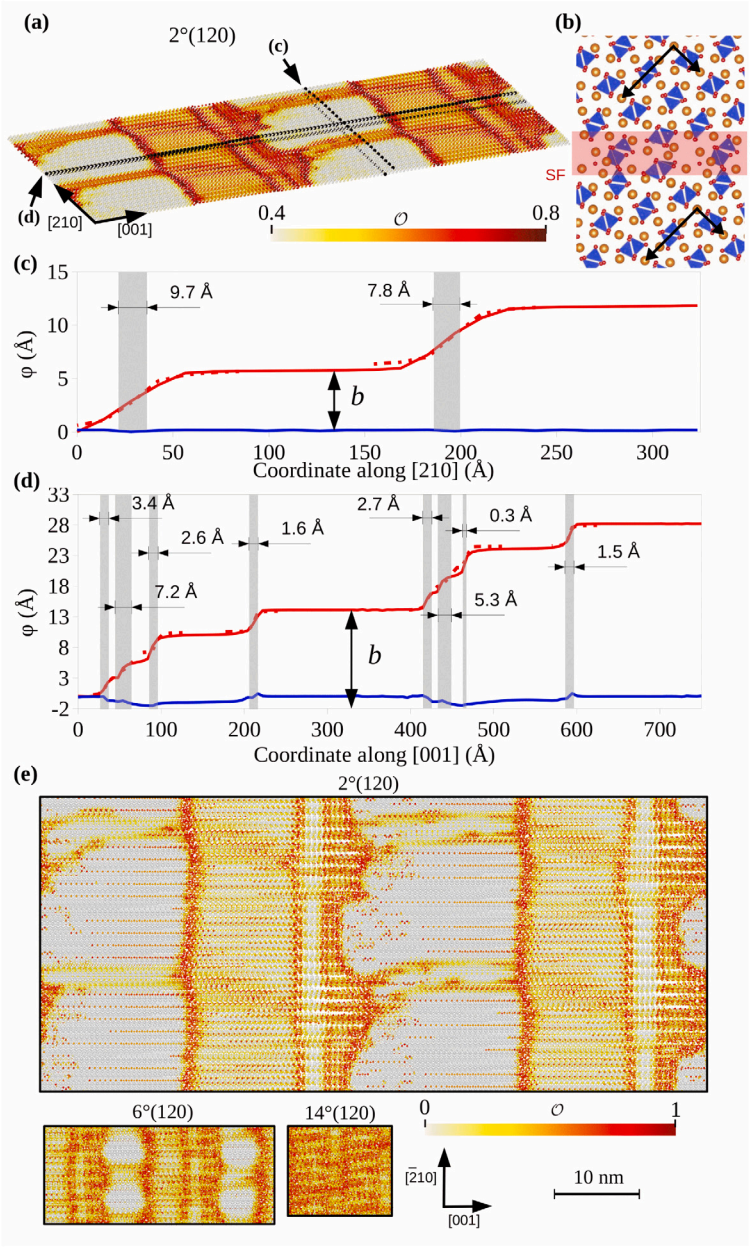

Fig. 7. Visualization and characterization of (120) twist GB. (a) Visualization of the 2°(120) GB (same color code as Fig. 3). (b) Atomic representation of the $\frac{1}{4}[\bar{2}10]$ stacking fault in (120), found between partial dislocations. This SF appears in shades of yellow–orange in other figures. (c) Disregistry associated with [001] screw dislocations. (d) Disregistry associated with $[\bar{2}10]$ dislocations, which are dissociated into four partials. (e) Top view of other low-angle (120) twist GB.

GSF [55] method is commonly used to study dislocation core structures, it has been shown to be less accurate for describing intracrystalline dislocations in forsterite [56]. However, our observations suggest that geometrical constraints imposed by the GB, which spread dislocation cores within the GB plane, may make the use of GSF more relevant in this context.

The (010) and (001) γ-surfaces used in the following for the analysis of low and very high angle GB have been computed using the interatomic potential (details on calculations and comparison with DFT are presented in supplementary materials). Fig. 8(a) presents the γ-surface in the (010) plane, which shows that translation of part of the crystal along the [100] or [001] lattice vectors results in configurations of very high energy (up to 2.5 J·m^{-2}). By following a curved path, as indicated by the black arrows, it is possible to reduce the energy of the stacking faults encountered along that path. Rather than forming perfect dislocations with narrow cores, it is more favorable for dislocations to spread, leading to a small edge component in the vicinity of their cores, which explains the spreading of [100] and [001] dislocations in low-angle (010) twist GB. The magnitude of this edge component (about 1 Å for [100] and 0.5 Å for [001]) matches what is observed in the disregistries (blue curves in Fig. 3).

By extending the GSF methodology, we computed the energy landscape of a (010) plane formed by two crystals misoriented by 180° with respect to the [010] axis (see Fig. 8(b)). In this case, translations along the [100] and [001] directions can occur without crossing high-energy barriers, explaining the narrow cores of [100] and [001] dislocations in near-180° (010) twist GB.

Fig. 8(c) shows the γ-surface in the (001) plane. Translation along [100] results in crossing a single maximum, and deviating slightly from the direct path may allow to reduce that energy (see black arrow in Fig. 8(c)). This is consistent with the fact that [100] dislocations have a narrow core with a small edge component in (001) GB. On the

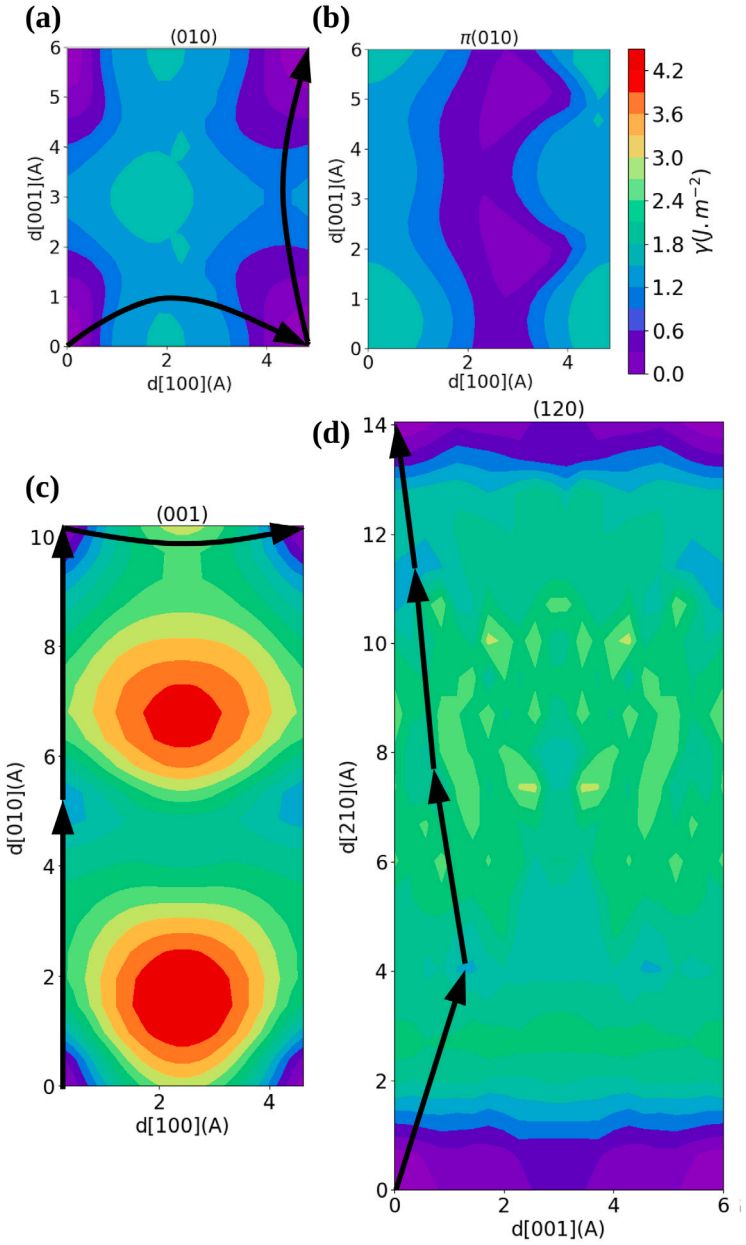

Fig. 8. γ-surfaces for (010) (a), π(010) (b), (001) (c) and (120) (d) planes computed using the interatomic potential [27]. Arrows represent the lowest energy paths for dislocation core spreading and dissociation, for the Burgers vectors observed in the corresponding low-angle twist GB.

contrary, translation along [010] leads to a local minimum at $\frac{1}{2}$[010]. This configuration corresponds to the ISF presented before, and confirms that it is metastable. In agreement with Frank's energy criterion, the presence of this ISF along the path indicates that it is favorable for [010] dislocations to dissociate into partial dislocations. Following the minimum energy path along the γ-surface, we find that the most favorable configuration is for the partial dislocations to have the same $\frac{1}{2}$[010] Burgers vector (represented by black arrows in Fig. 8(c)), as observed in our low-angle (001) twist GB.

The energy landscape of (001) plane formed by two crystal misoriented of 180° with respect to the [001] axis have the same shape than the γ-surface of the (001) plane and is not presented here. The only differences are in the absolute energy values and notably the minimum energy, which corresponds to that of the π(001) SF. This close similarity between the (001) γ-surface and the π(001) energy landscape explains the nearly identical core structures of [100] and $\frac{1}{2}$[010] dislocations in low-angle and near-180° twist GB (see Figs. 5 and 6).

The γ-surface of the (120) plane presented in Fig. 8(d) is irregular and presents abrupt energy variations. Nevertheless, translation along [001] can occur without crossing any high energy barrier leading to the relatively narrow core of the [001] dislocations observed in our (120) low angle GB. Different local energy minima can be found along the [$\bar{2}$10] direction, and we propose a dissociation reaction illustrated by the black arrows in Fig. 8(d). This dissociation reaction is such that all partial dislocations have a screw component almost equal to $\frac{1}{4}$[$\bar{2}$10] and a small edge component ($<\frac{1}{6}$[001]), which corresponds to the measured disregistries (see Fig. 7(c) and (d)).

To summarize, in all of the low-angle and near-180° twist GB investigated here and at the difference with intracrystalline dislocations, the GSF allows to understand both interface GND core structures and dissociations observed in the GB. This emphasizes the strong impact of the geometrical constraints due to the GB on the nature and structure of interface GND. In fact, as long as a low energetical solution can be found from the GSF, the corresponding interface GND can be formed

although this type of dislocation (or even its core structure) could never have existed in the intracrystalline form (for instance the $\frac{1}{4}[\bar{2}10]$ partial dislocations).

It is worth noticing that the above conclusions also hold for dissociation width. In fact, knowing the energy of the ISF, one can use the elastic theory of dislocations to estimate the dissociation width [57] namely $d_{\text{th}} = \mu b^2/(2\pi\gamma^{\text{ISF}})$, which yields $d_{\text{th}} \approx 29$ and 31 Å for $\frac{1}{2}[010]$ dislocations in (001) GB and $\frac{1}{4}[\bar{2}10]$ dislocations in (120) GB, respectively. These values differ from the ones measured in our simulated GB. However this calculation assumes a single dissociated dislocation in an otherwise perfect crystal. In low-angle and near-180° GB, the misorientation angle between the two crystals imposes its own periodicity and constraints. As a result, dissociation width in GB is also mainly controlled by geometric constraints, rather than by the SF energy.

These findings emphasize how carefully should be interpreted the HRTEM investigations of dislocation core structures. Although scarce for silicate materials, these studies generally focus on low angle GB dislocations [58–61], and their structures could then be not representative of the intracrystalline ones. Nevertheless, further experimental/numerical investigations are needed to infer any construction bias in our conclusions. In fact, while low-angle GB are formed by continuous processes (e.g. dislocation accumulation), our construction methodology imposes the misorientation angle in a discontinuous way which may impact the dislocation types or core structures composing the GB.

In all of the low angle twist GB analyzed here, a common feature is the more or less pronounced spreading of the dislocation cores in the GB plane. Except TEM study showing image of low angle GB in garnet (also a silicate material) with an array of dislocations extremely spread in the GB plane [62], we do not find any other study putting forward such characteristic. A noticeable exception can be found in (111) low angle twist GB in FCC for which a spreading of the perfect interface GND in the GB plane seems possible [23]. In the other hand, it seems also possible in FCC for the interface GND to be spread in their slip planes, even if the later is not parallel to the GB plane [34].

4.2. Elastic model and limit between low- and high-angle GB

Evolution of the GB microstructure with misorientation are presented for the (010) plane in Figs. 3(d) and 4(d), for the (001) plane in Figs. 5(e) and 6(e) and for (120) plane in Fig. 7(e).

At low misorientation angles, regardless of the GB plane, the distance between the dislocations forming the GB, whether they are perfect or partial, decreases as the misorientation angle increases. However, for misorientations greater than 10°, it becomes increasingly difficult to distinguish individual dislocations within the GB.

In the case of near-180° (010) and (001) GB, the dislocation spacing decreases as the misorientation angle increases. Notably, the distance between dislocations is identical for misorientations θ and $180° - \theta$ (for small values of θ). For misorientation angles less than 170°, individual dislocations can no longer be distinguished.

The measured dislocation spacing and core radius values for different GB, along with the dislocation distances predicted by elastic theory (Eq. (4)), where θ has been replaced by $180° - \theta$ for near-180° GBs, are presented in Fig. 9.

The dislocation distances predicted by the Frank–Bilby equation closely match the measured distances for all GB planes and dislocations. When we extrapolate Eq. (4), we find that the dislocation core radii intersect with the dislocation distances for misorientation angles ranging between 17° (for [100] dislocations) and 40° (for $\frac{1}{2}[010]$ dislocations).

The different distances between dislocations, average core radii and SF energies from our simulations (see. Table 1) have been used as input parameters in the elastic model presented in the methods (Eq. (5)). The theoretical energies thus obtained are represented as dashed lines in Fig. 1. The elastic model produces energies comparable to those from atomistic simulations, only for low-angle GB where $\theta < 10°$ or $\theta > 170°$. Surprisingly, the elastic model (Eq. (5)) fails to predict energies of

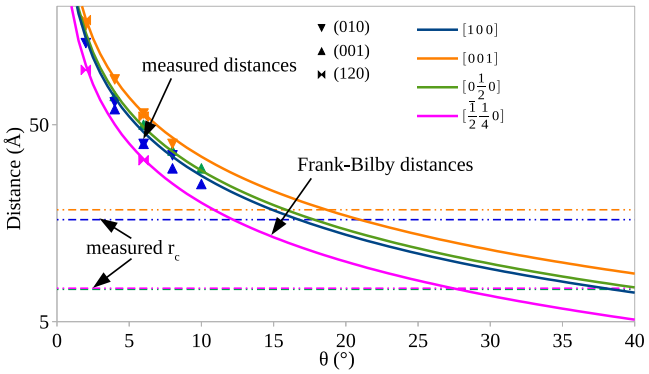

Fig. 9. Measured distances (symbols) and average core diameter (dashed lines) between different dislocation types in low angle twist GB. The solid lines correspond to the dislocation distances computed using Eq. (4).

low-angle (010) GB (in blue in Fig. 1). This may be due to the fact that dislocations in this type of GB tend to spread and form complex junctions, as shown in Fig. 3(a) and (d), a situation unaccounted for by the elastic model.

The critical misorientation angle at which dislocation cores start to overlap depends on the dislocation type and ranges from 18° for [100] and [001] dislocations to more than 30° for $[0\frac{1}{2}0]$ and $[\frac{\bar{1}}{2}\frac{1}{4}0]$ dislocations (refer to Fig. 9). Even in the case of the lowest angle, this critical misorientation angle significantly exceeds the threshold at which individual dislocations can no longer be distinguished, as shown in Section 3.2. Moreover, these critical angles also surpass the limit beyond which the elastic model (Eq. (5)) no longer accurately predicts GB energies. However, these values are consistent with the findings of [19], who reported a transition angle of 20° in forsterite.

4.3. High-angle GB

The fact that the GB energy curves do not present cusps or particular points (except for the 90°(001)) observed in this study has also been noticed in the review paper of [20] and attributed to the low symmetry of the forsterite structure. Even if it is well accepted that high coincidence GB have not necessarily low energy, the cusps observed in the GB energy curves in simpler structures, such as cubic or hexagonal ones, are often associated with low Σ GB [24]. The weak coincidence nature of low-symmetry crystals, such as forsterite, could also be responsible for the absence of periodic patterns in high angle GB which is also observed in higher symmetry crystals such as body centered cubic [24].

The fact that any particular features are not observed in high angle GB should not be necessarily interpreted as the absence of periodic patterns. Indeed, the bond orientational parameter used here (see Section 2.4) allows to distinguish between perfect crystal and disordered local atomic environments. However, it may fail to highlight such fine features in a strongly disordered atomic arrangement. Refinement of the current bond orientational parameter may resolve this issue.

The case of the 90°(001) GB, which is the only particular high angle GB observed in this study, could be linked to the fact that the a lattice parameter is almost the half of the b one, which may lead in the case of a 90° rotation to a match between the unit cells, even if the calculated Σ value for the unrelaxed GB is relatively high (105).

A common feature between GB in forsterite and in higher symmetry crystals is the positive correlation between GB energy and excess volume. This relation has also been observed in forsterite GB [30] as well as the positive correlation of excess volume with diffusion rate [63].

Finally, the high-angle GB investigated here contain a sensible concentration of non-silicate oxygen sites (cf Fig. 2(b)) which may diffuse quicker than oxygen bonded with silicon ions and contribute to the higher oxygen diffusion rate in GB compared to bulk observed

experimentally [64]. Moreover, these free oxygens may be easily protonated, contributing to the water storage in mantle rocks on GB as explained in [30].

5. Conclusion

We have modeled twist grain boundaries in Mg_2SiO_4 forsterite using atomic-scale simulations. To the first order, GB energies follow the same ordering as their free surface counterparts. We find that microscopic degrees of freedom, such as translation of the grains with respect to one another, have little influence on the GB energies and structures.

Low-angle twist GB structures are accommodated by arrays of interface screw GND.

We showed that the core structure of these defects strongly varies depending on the specific crystallographic plane with which they are associated. For instance, there are notable distinctions in the core structures of [100] interface GND in (010) and (001) low-angle twist GB. It is important to emphasize that these interface GND differ significantly from their intracrystalline counterparts. This underlines the necessity for cautious interpretation when inferring core structures of low-angle GB dislocations in experimental studies.

Our investigation has also demonstrated the effectiveness of the GSF concept in understanding the type and structure of interface GND. Furthermore, our findings highlight that, if a low-energy solution is attainable via GSF, the corresponding interface GND can be formed, even if such dislocations (or their specific core structures) may not exist in an intracrystalline context—such as the case of the $\frac{1}{4}[\bar{2}10]$ partial dislocations.

The present work focused on static properties of pristine twist GB. An additional degree of freedom may have an important influence on these results, the possible deviation from stoichiometry. Our previous work on tilt GB [30] demonstrated that ions close to GB are often associated with negative vacancy formation energy. It would be of high importance to model the formation and segregation of vacancies and partial Schottky defects (MgO or SiO_2) into twist GB as well. In addition, inside the Earth's upper mantle, forsterite is submitted to pressures up to 15 GPa and temperatures up to 1000 K. It would therefore be interesting to study the effects of pressure and temperature on GB structures and energies. Finally, it would be interesting to investigate dynamic properties of those GB, in particular ion diffusion or the mechanical response to shear, as these are expected to control the rheology of this phase.

CRediT authorship contribution statement

Jean Furstoss: Conceptualization, Data curation, Investigation, Methodology, Software, Visualization, Writing – original draft, Writing – review & editing. **Pierre Hirel:** Conceptualization, Funding acquisition, Investigation, Methodology, Supervision, Validation, Writing – review & editing. **Philippe Carrez:** Investigation, Validation, Writing – review & editing. **Karine Gouriet:** Investigation, Writing – review & editing. **Victoire Meko-Fotso:** Investigation, Writing – review & editing. **Patrick Cordier:** Funding acquisition, Investigation, Supervision, Validation, Writing – original draft, Writing – review & editing.

Declaration of competing interest

The authors declare that they have no known competing financial interests or personal relationships that could have appeared to influence the work reported in this paper.

Data availability

All the data used for plotting the different figures presented in this work, as well as the LAMMPS scripts used for the different computations, are available from the authors upon request. The code used for the computation of the bond orientational parameter presented in section 2.4, is available at https://github.com/JeanFurstoss/AtomHIC.

Acknowledgments

This project has received funding from the French government through the Programme Investissement d'Avenir (I-SITE ULNE/ANR-16-IDEX-0004 ULNE) managed by the Agence Nationale de la Recherche, France, under the project name NuMoGO, and from the European Research Council (ERC) under the European Union's Horizon 2020 research and innovation programme under grant agreement No 787198 – TimeMan. Computational resources have been provided by the DSI at Université de Lille.

Appendix A. Supplementary data

Supplementary material related to this article can be found online at https://doi.org/10.1016/j.commatsci.2023.112768.

References

[1] Greg Hirth, David L. Kohlstedt, Experimental constraints on the dynamics of the partially molten upper mantle: Deformation in the diffusion creep regime, J. Geophys. Res. Solid Earth 100 (B2) (1995) 1981–2001, http://dx.doi.org/10.1029/94JB02128.

[2] Shenghua Mei, David L. Kohlstedt, Influence of water on plastic deformation of olivine aggregates: 1. diffusion creep regime, J. Geophys. Res. Solid Earth 105 (B9) (2000) 21457–21469, http://dx.doi.org/10.1029/2000JB900179.

[3] Katharina Marquardt, Quentin M Ramasse, Christian Kisielowski, Richard Wirth, Diffusion in yttrium aluminium garnet at the nanometer-scale: Insight into the effective grain boundary width, Am. Mineral. 96 (10) (2011) 1521–1529, http://dx.doi.org/10.2138/am.2011.3625.

[4] Katharina Marquardt, Elena Petrishcheva, Emmanuel Gardés, Richard Wirth, Rainer Abart, Wilhelm Heinrich, Grain boundary and volume diffusion experiments in yttrium aluminium garnet bicrystals at 1,723 k: a miniaturized study, Contributions Mineral. Petrol. 162 (2011) 739–749, http://dx.doi.org/10.1007/s00410-011-0622-7.

[5] Shun I. Karato, Grain growth kinetics in olivine aggregates, Tectonophysics 168 (4) (1989) 255–273, http://dx.doi.org/10.1016/0040-1951(89)90221-7.

[6] Takehiko Hiraga, Chihiro Tachibana, Naoki Ohashi, Satoru Sano, Grain growth systematics for forsterite±enstatite aggregates: Effect of lithology on grain size in the upper mantle, Earth Planet. Sci. Lett. 291 (1–4) (2010) 10–20, http://dx.doi.org/10.1016/j.epsl.2009.12.026.

[7] Robert W. Balluffi, Adrian Sutton, Why should we be interested in the atomic structure of interfaces? in: Materials Science Forum, Vol. 207, Trans Tech Publ, 1996, pp. 1–12, http://dx.doi.org/10.4028/www.scientific.net/MSF.207-209.1.

[8] Jian Han, Vaclav Vitek, David J. Srolovitz, Grain-boundary metastability and its statistical properties, Acta Mater. 104 (2016) 259–273, http://dx.doi.org/10.1016/j.actamat.2015.11.035.

[9] Pierre Hirel, Gabriel Franck Bouobda Moladje, Philippe Carrez, Patrick Cordier, Systematic theoretical study of [001] symmetric tilt grain boundaries in MgO from 0 to 120 GPa, Phys. Chem. Miner. 46 (1) (2019) 37–49, http://dx.doi.org/10.1007/s00269-018-0985-7.

[10] Arslan B. Mazitov, Artem R. Oganov, Grain boundaries in minerals: Atomic structure, phase transitions, and effect on strength of polycrystals, 2021, http://dx.doi.org/10.48550/arXiv.2106.13570, arXiv preprint arXiv:2106.13570.

[11] Patrick R Cantwell, Ming Tang, Shen J Dillon, Jian Luo, Gregory S Rohrer, Martin P Harmer, Grain boundary complexions, Acta Mater. 62 (2014) 1–48, http://dx.doi.org/10.1016/j.actamat.2013.07.037.

[12] Thorsten Meiners, Timofey Frolov, Robert E Rudd, Gerhard Dehm, Christian H Liebscher, Observations of grain-boundary phase transformations in an elemental metal, Nature 579 (7799) (2020) 375–378, http://dx.doi.org/10.1038/s41586-020-2082-6.

[13] Vivekanand Muralikrishnan, He Liu, Lin Yang, Bryan Conry, Christopher J Marvel, Martin P Harmer, Gregory S Rohrer, Michael R Tonks, Robert M Suter, Carl E Krill III, et al., Observations of unexpected grain boundary migration in SrTiO3, Scr. Mater. 222 (2023) 115055, http://dx.doi.org/10.1016/j.scriptamat.2022.115055.

[14] Pierre Hirel, Philippe Carrez, Patrick Cordier, Why do compact grain boundary complexions prevail in rock-salt materials? Acta Mater. 240 (2022) 118297, http://dx.doi.org/10.1016/j.actamat.2022.118297.

[15] Hosni Idrissi, Philippe Carrez, Patrick Cordier, On amorphization as a deformation mechanism under high stresses, Curr. Opin. Solid State Mater. Sci. 26 (1) (2022) 100976, http://dx.doi.org/10.1016/j.cossms.2021.100976.

[16] Johannes Duyster, Bernhard Stöckhert, Grain boundary energies in olivine derived from natural microstructures, Contributions Mineral. Petrol. 140 (5) (2001) 567–576, http://dx.doi.org/10.1007/s004100000200.

[17] William T. Read, WJPR Shockley, Dislocation models of crystal grain boundaries, Phys. Rev. 78 (3) (1950) 275, http://dx.doi.org/10.1103/PhysRev.78.275.

[18] Hongzhan Fei, Sanae Koizumi, Naoya Sakamoto, Minako Hashiguchi, Hisayoshi Yurimoto, Katharina Marquardt, Nobuyoshi Miyajima, Daisuke Yamazaki, Tomoo Katsura, New constraints on upper mantle creep mechanism inferred from silicon grain-boundary diffusion rates, Earth Planet. Sci. Lett. 433 (2016) 350–359, http://dx.doi.org/10.1016/j.epsl.2015.11.014.

[19] Stefan Heinemann, Richard Wirth, Matthias Gottschalk, Georg Dresen, Synthetic [100] tilt grain boundaries in forsterite: 9.9 to 21.5, Phys. Chem. Miner. 32 (4) (2005) 229–240, http://dx.doi.org/10.1007/s00269-005-0448-9.

[20] Katharina Marquardt, Ulrich H. Faul, The structure and composition of olivine grain boundaries: 40 years of studies, status and current developments, Phys. Chem. Miner. 45 (2) (2018) 139–172, http://dx.doi.org/10.1007/s00269-017-0935-9.

[21] Dipta B. Ghosh, Bijaya B. Karki, First principles simulations of the stability and structure of grain boundaries in Mg_2SiO_4 forsterite, Phys. Chem. Miner. 41 (3) (2014) 163–171, http://dx.doi.org/10.1007/s00269-013-0633-1.

[22] Omar Adjaoud, Katharina Marquardt, Sandro Jahn, Atomic structures and energies of grain boundaries in Mg_2SiO_4 forsterite from atomistic modeling, Phys. Chem. Miner. 39 (9) (2012) 749–760, http://dx.doi.org/10.1007/s00269-012-0529-5.

[23] Carolina Baruffi, Christian Brandl, On the structure of (111) twist grain boundaries in diamond: atomistic simulations with tersoff-type interatomic potentials, Acta Mater. 215 (2021) 117055, http://dx.doi.org/10.1016/j.actamat.2021.117055.

[24] Ya-Xin Feng, Jia-Xiang Shang, Zeng-Hui Liu, Guang-Hong Lu, The energy and structure of (1 1 0) twist grain boundary in tungsten, Appl. Surf. Sci. 357 (2015) 262–267, http://dx.doi.org/10.1016/j.apsusc.2015.08.265.

[25] Qing Yin, Zhiqiang Wang, Rajiv Mishra, Zhenhai Xia, Atomic simulations of twist grain boundary structures and deformation behaviors in aluminum, Aip Adv. 7 (1) (2017) 015040, http://dx.doi.org/10.1063/1.4975042.

[26] Shuyang Dai, Yang Xiang, David J. Srolovitz, Structure and energy of (1 1 1) low-angle twist boundaries in Al, Cu and Ni, Acta Mater. 61 (4) (2013) 1327–1337, http://dx.doi.org/10.1016/j.actamat.2012.11.010.

[27] Alfonso Pedone, Gianluca Malavasi, M Cristina Menziani, Alastair N Cormack, Ulderico Segre, A new self-consistent empirical interatomic potential model for oxides, silicates, and silica-based glasses, J. Phys. Chem. B 110 (24) (2006) 11780–11795, http://dx.doi.org/10.1021/jp0611018.

[28] James W. Eastwood, Roger Williams Hockney, D.N. Lawrence, P3M3DP—The three-dimensional periodic particle-particle/particle-mesh program, Comput. Phys. Comm. 19 (2) (1980) 215–261.

[29] Pierre Hirel, Jean Furstoss, Philippe Carrez, A critical assessment of interatomic potentials for modelling lattice defects in forsterite Mg_2SiO_4 from 0 to 12 GPa, Phys. Chem. Miner. 48 (12) (2021) 46, http://dx.doi.org/10.1007/s00269-021-01170-6.

[30] Jean Furstoss, Pierre Hirel, Philippe Carrez, Patrick Cordier, Complexions and stoichiometry of the 60.8°//[100](011) symmetrical tilt grain boundary in Mg_2SiO_4 forsterite: A combined empirical potential and first-principles study, Am. Mineral. 107 (11) (2022) 2034–2043, http://dx.doi.org/10.2138/am-2022-8420.

[31] Steve Plimpton, Fast parallel algorithms for short-range molecular dynamics, J. Comput. Phys. 117 (1) (1995) 1–19, http://dx.doi.org/10.1006/jcph.1995.1039.

[32] Marco Bruno, Francesco R Massaro, Mauro Prencipe, Raffaella Demichelis, M De La Pierre, Fabrizio Nestola, Ab initio calculations of the main crystal surfaces of forsterite (Mg_2SiO_4): A preliminary study to understand the nature of geochemical processes at the olivine interface, J. Phys. Chem. C 118 (5) (2014) 2498–2506, http://dx.doi.org/10.1021/jp409837d.

[33] Norman A. Gjostein, Frederick N. Rhines, Absolute interfacial energies of [001] tilt and twist grain boundaries in copper, Acta Metall. 7 (5) (1959) 319–330, http://dx.doi.org/10.1016/0001-6160(59)90198-1.

[34] Luchan Zhang, Yejun Gu, Yang Xiang, Energy of low angle grain boundaries based on continuum dislocation structure, Acta Mater. 126 (2017) 11–24, http://dx.doi.org/10.1016/j.actamat.2016.12.035.

[35] Frederick Charles Frank, Report of the Symposium on the Plastic Deformation of Crystalline Solids, Vol. 150, Carnegie Institute of Technology, Pittsburgh, 1950.

[36] Bruce Alexander Bilby, R. Bullough, Edwin Smith, Continuous distributions of dislocations: a new application of the methods of non-Riemannian geometry, Proc. R. Soc. A 231 (1185) (1955) 263–273, http://dx.doi.org/10.1098/rspa.1955.0171.

[37] Jinbo Yang, Yasuyoshi Nagai, Masayuki Hasegawa, Use of the Frank–Bilby equation for calculating misfit dislocation arrays in interfaces, Scr. Mater. 62 (7) (2010) 458–461, http://dx.doi.org/10.1016/j.scriptamat.2009.12.011.

[38] Akira Otsuki, Energies of (001) twist grain boundaries in silicon, Acta Mater. 49 (10) (2001) 1737–1745, http://dx.doi.org/10.1016/S1359-6454(01)00090-8.

[39] Cynthia L. Kelchner, S.J. Plimpton, J.C. Hamilton, Dislocation nucleation and defect structure during surface indentation, Phys. Rev. B 58 (17) (1998) 11085, http://dx.doi.org/10.1103/PhysRevB.58.11085.

[40] J. Dana Honeycutt, Hans C. Andersen, Molecular dynamics study of melting and freezing of small lennard-jones clusters, J. Phys. Chem. 91 (19) (1987) 4950–4963.

[41] Alexander Stukowski, Karsten Albe, Extracting dislocations and non-dislocation crystal defects from atomistic simulation data, Modelling Simul. Mater. Sci. Eng. 18 (8) (2010) 085001, http://dx.doi.org/10.1088/0965-0393/18/8/085001.

[42] Paul J. Steinhardt, David R. Nelson, Marco Ronchetti, Bond-orientational order in liquids and glasses, Phys. Rev. B 28 (2) (1983) 784, http://dx.doi.org/10.1103/PhysRevB.28.784.

[43] Sebastian von Alfthan, Peter D Haynes, Kimmo Kaski, Adrian P Sutton, Are the structures of twist grain boundaries in silicon ordered at 0 K? Phys. Rev. Lett. 96 (5) (2006) 055505, http://dx.doi.org/10.1103/PhysRevLett.96.055505.

[44] Alvin L-S Chua, Nicole A Benedek, Lin Chen, Mike W Finnis, Adrian P Sutton, A genetic algorithm for predicting the structures of interfaces in multicomponent systems, Nat. Mater. 9 (5) (2010) 418–422, http://dx.doi.org/10.1038/nmat2712.

[45] Gang Lu, The Peierls—Nabarro model of dislocations: a venerable theory and its current development, in: Handbook of Materials Modeling: Methods, Springer, 2005, pp. 793–811.

[46] David L. Kohlstedt, Christopher Goetze, William B Durham, John B Vander Sande, New technique for decorating dislocations in olivine, Science 191 (4231) (1976) 1045–1046, http://dx.doi.org/10.1126/science.191.4231.1045.

[47] Alexandre Mussi, Patrick Cordier, Sylvie Demouchy, Characterization of dislocation interactions in olivine using electron tomography, Phil. Mag. 95 (4) (2015) 335–345, http://dx.doi.org/10.1080/14786435.2014.1000996.

[48] Daniel L. Ricoult, David L. Kohlstedt, Structural width of low-angle grain boundaries in olivine, Phys. Chem. Miner. 9 (3–4) (1983) 133–138, http://dx.doi.org/10.1007/BF00308370.

[49] Yves Guéguen, Dislocations in naturally deformed terrestrial olivine: classification, interpretation, applications, Bull. Mineral. 102 (2) (1979) 178–184.

[50] William B. Durham, Christopher Goetze, Brenda Jean Blake, Plastic flow of oriented single crystals of olivine: 2. Observations and interpretations of the dislocation structures, J. Geophys. Res. 82 (36) (1977) 5755–5770, http://dx.doi.org/10.1029/JB082i036p05755.

[51] Srinivasan Mahendran, Philippe Carrez, Sebastien Groh, Philippe Cordier, Dislocation modelling in Mg_2SiO_4 forsterite: an atomic-scale study based on the THB1 potential, Modelling Simul. Mater. Sci. Eng. 25 (5) (2017) 054002, http://dx.doi.org/10.1088/1361-651X/aa6efa.

[52] Srinivasan Mahendran, Philippe Carrez, Patrick Cordier, The core structure of screw dislocations with [001] Burgers vector in Mg_2SiO_4 olivine, C. R. Phys. 22 (S3) (2021) 7–18, http://dx.doi.org/10.5802/crphys.27.

[53] Kiyoshi Fujino, Hiroyuki Nakazaki, Hitoshi Momoi, Shun-ichiro Karato, David L Kohlstedt, TEM observation of dissociated dislocations with b=[010] in naturally deformed olivine, Phys. Earth Planet. Inter. 78 (1–2) (1993) 131–137, http://dx.doi.org/10.1016/0031-9201(93)90089-R.

[54] Christopher Goetze, David L. Kohlstedt, Laboratory study of dislocation climb and diffusion in olivine, J. Geophys. Res. 78 (26) (1973) 5961–5971, http://dx.doi.org/10.1029/JB078i026p05961.

[55] Vaclav Vitek, Intrinsic stacking faults in body-centred cubic crystals, Phil. Mag. 18 (154) (1968) 773–786, http://dx.doi.org/10.1080/14786436808227500.

[56] Philippe Carrez, Andrew M Walker, Arnaud Metsue, Patrick Cordier, Evidence from numerical modelling for 3D spreading of [001] screw dislocations in Mg_2SiO_4 forsterite, Phil. Mag. 88 (16) (2008) 2477–2485, http://dx.doi.org/10.1080/14786430802363804.

[57] John Price Hirth, Jens Lothe, Toshio Mura, Theory of dislocations, J. Appl. Mech. 50 (2) (1983) 476.

[58] Zaoli Zhang, Wilfried Sigle, Wolfgang Kurtz, Manfred Rühle, Electronic and atomic structure of a dissociated dislocation in SrTiO3, Phys. Rev. B 66 (21) (2002) 214112, http://dx.doi.org/10.1103/PhysRevB.66.214112.

[59] Naoya Shibata, Matthew F Chisholm, Atsutomo Nakamura, Stephen J Pennycook, Takeshi Yamamoto, Yuichi Ikuhara, Nonstoichiometric dislocation cores in α-alumina, Science 316 (5821) (2007) 82–85, http://dx.doi.org/10.1126/science.113615.

[60] Zhongchang Wang, Mitsuhiro Saito, Keith P McKenna, Yuichi Ikuhara, Polymorphism of dislocation core structures at the atomic scale, Nat. Commun. 5 (1) (2014) 3239, http://dx.doi.org/10.1038/ncomms4239.

[61] Rong Sun, Zhongchang Wang, Naoya Shibata, Yuichi Ikuhara, A dislocation core in titanium dioxide and its electronic structure, Rsc Adv. 5 (24) (2015) 18506–18510, http://dx.doi.org/10.1039/C4RA15278F.

[62] Violaine Voegelé, Patrick Cordier, Violaine Sautter, Thomas G. Sharp, Jean Marc Lardeaux, Fernando O Marques, Plastic deformation of silicate garnets: II. Deformation microstructures in natural samples, Phys. Earth Planet. Inter. 108 (4) (1998) 319–338, http://dx.doi.org/10.1016/S0031-9201(98)00111-3.

[63] Johannes Wagner, Omar Adjaoud, Katharina Marquardt, Sandro Jahn, Anisotropy of self-diffusion in forsterite grain boundaries derived from molecular dynamics simulations, Contributions Mineral. Petrol. 171 (2016) 1–9, http://dx.doi.org/10.1007/s00410-016-1308-y.

[64] Hisayoshi Yurimoto, Masana Morioka, Hiroshi Nagasawa, Oxygen self-diffusion along high diffusivity paths in forsterite, Geochem. J. 26 (4) (1992) 181–188, http://dx.doi.org/10.2343/geochemj.26.181.